Scripta Materialia 142 (2018) 116–120

Contents lists available at ScienceDirect

Scripta Materialia

journal homepage: www.elsevier.com/locate/scriptamat

Regular article

# A new class of high-entropy perovskite oxides

Sicong Jiang, Tao Hu [1], Joshua Gild, Naixie Zhou, Jiuyuan Nie, Mingde Qin, Tyler Harrington, Kenneth Vecchio, Jian Luo *

*Department of NanoEngineering, University of California, San Diego, La Jolla, CA 92093, USA*

ARTICLE INFO

*Article history:*
Received 8 July 2017
Received in revised form 8 August 2017
Accepted 23 August 2017
Available online xxxx

*Keywords:*
High-entropy ceramics
Perovskite
Phase stability

ABSTRACT

A new class of high-entropy perovskite oxides (*i.e.*, multiple-cation solid solutions with high configurational entropies) has been synthesized. Six of the 13 compositions examined, including $Sr(Zr_{0.2}Sn_{0.2}Ti_{0.2}Hf_{0.2}Mn_{0.2})O_3$, $Sr(Zr_{0.2}Sn_{0.2}Ti_{0.2}Hf_{0.2}Nb_{0.2})O_3$, $Ba(Zr_{0.2}Sn_{0.2}Ti_{0.2}Hf_{0.2}Ce_{0.2})O_3$, $Ba(Zr_{0.2}Sn_{0.2}Ti_{0.2}Hf_{0.2}Y_{0.2})O_{3-x}$, $Ba(Zr_{0.2}Sn_{0.2}Ti_{0.2}Hf_{0.2}Nb_{0.2})O_3$ and $(Sr_{0.5}Ba_{0.5})(Zr_{0.2}Sn_{0.2}Ti_{0.2}Hf_{0.2}Nb_{0.2})O_3$, can form homogeneous single solid-solution phases. Goldschmidt's tolerance factor, instead of cation-size difference, influences the formation and temperature-stability of single cubic perovskite solid solutions. This new class of multicomponent (high-entropy) perovskite solid solutions with distinct and highly-tunable chemistries can enable simultaneous tailoring of multiple properties and potentially lead to new functionality.



Recently, the research of high-entropy alloys (HEAs), also known as "multi-principal element alloys," has received great attentions because they possess a variety of excellent mechanical and physical properties [1–3]. The majority of HEAs are metals that have simple FCC, BCC or HCP structures [1–3]. To date, only a couple of high-entropy ceramic structures have been successfully fabricated in the bulk form. First, Rost et al. reported an entropy-stabilized rocksalt (FCC) oxide ($(Mg_{0.2}Ni_{0.2}Co_{0.2}Cu_{0.2}Zn_{0.2}O$) in 2015 [4] and its derivative materials doped with Li and Ga cations showed promising ion-conducting and dielectric properties [5,6]. Second, high-entropy metal diborides with a layered $AlB_2$ crystal structure, which contains alternating 2-D high-entropy cationic/metallic solid-solution layers and covalent boron nets, were synthesized as a new class of ultra-high temperature ceramics [7]. In this study, we successfully synthesized, for the first time to our knowledge, yet another new class of high-entropy perovskite oxides, which can potentially have unique physical properties and allow simultaneous tailoring of multiple physical properties due to their distinct and highly-tunable chemistries. This study also represents the first report of high-entropy materials that have a complex ionic crystal structure with at least two cation sublattices.

An $ABO_3$ perovskite oxide contains a 12-fold coordinated A cation sublattice, a 6-fold coordinated B cation sublattice, and an octahedral oxygen anion sublattice. In 1926, Goldschmid introduced a structural "tolerance factor" [8] to predict the stability of perovskite:

$$t = \frac{R_A + R_O}{\sqrt{2}\,(R_B + R_O)} \tag{1}$$

where $R_A$, $R_B$ and $R_O$, respectively, are the radii of A cation, B cation and oxygen anion. A cubic phase is likely stable if $0.9 \le t \le 1.0$, while a hexagonal or tetragonal phase may form if $t > 1.0$ and an orthorhombic or rhombohedral phase may form if $t < 0.9$ [9]. $ABO_3$ perovskite oxides have excellent and diverse physical properties for applications in many different areas, *e.g.*, they can be used as cathode materials for solid oxide fuel cells [10], proton conductors [11], photocatalysts [12], dielectrics [13–16], and ferroelectric and multiferroic materials [17–21]. They can also serve as the base crystal structure for realizing 2-D electron gas and high-temperature superconductivity [16,22–24]. Doping with multiple cations may allow simultaneous tailoring of multiple physical properties of $ABO_3$ perovskite oxides to meet challenging requirements of real applications, as exemplified by a couple of recent studies for fuel cells [25–27]. In this study, we further extend $ABO_3$ perovskite solid solutions to high-entropy compositions, where we successfully synthesized six single-phase, high-entropy, perovskite oxides (among 13 compositions that we have examined; Table 1), *i.e.*, $Sr(Zr_{0.2}Sn_{0.2}Ti_{0.2}Hf_{0.2}Mn_{0.2})O_3$, $Sr(Zr_{0.2}Sn_{0.2}Ti_{0.2}Hf_{0.2}Nb_{0.2})O_3$, $Ba(Zr_{0.2}Sn_{0.2}Ti_{0.2}Hf_{0.2}Ce_{0.2})O_3$, $Ba(Zr_{0.2}Sn_{0.2}Ti_{0.2}Hf_{0.2}Y_{0.2})O_{3-x}$, $Ba(Zr_{0.2}Sn_{0.2}Ti_{0.2}Hf_{0.2}Nb_{0.2})O_3$ and $(Sr_{0.5}Ba_{0.5})(Zr_{0.2}Sn_{0.2}Ti_{0.2}Hf_{0.2}Nb_{0.2})O_3$, and we have further shown that the Goldschmidt's tolerance factor correlates with the formation and temperature-stability of these multi-cation perovskite solid-solution phases.

* Corresponding author.
*E-mail address:* jluo@alum.mit.edu (J. Luo).
[1] Current Address: School of Materials Science and Engineering, Central South University, Changsha, Hunan 410083, China.

http://dx.doi.org/10.1016/j.scriptamat.2017.08.040
1359-6462/

**Table 1**
Summary of the key findings of all 13 compositions examined. To roughly indicate the amounts of secondary phases, "trace" means that a secondary phase could not be identified by XRD but EDXS mapping show composition non-uniformity. If a secondary phase can be detected by XRD and the intensity of its strongest XRD peak is <6% of that of the perovskite (110) peak, we label "minor" in the table; otherwise, "major" implies that the intensity ratio of the maximum XRD peaks is >6%.

| | Composition | Secondary phase? | | | $\delta(R_B)$ | Tolerance factor $t$ |
|---|---|---|---|---|---|---|
| | | 1300 °C | 1400 °C | 1500 °C | | |
| #S0 | $Sr(Zr_{0.25}Sn_{0.25}Ti_{0.25}Hf_{0.25})O_3$ | Minor | Minor | Major | 6.7% | 0.97 |
| #S1 | $Sr(Zr_{0.2}Sn_{0.2}Ti_{0.2}Hf_{0.2}Mn_{0.2})O_3$ | Minor | Trace | No | 11.2% | 0.99 |
| #S2 | $Sr(Zr_{0.2}Sn_{0.2}Ti_{0.2}Hf_{0.2}Ce_{0.2})O_3$ | Major | Major | Major | 11.9% | 0.95 |
| #S3 | $Sr(Zr_{0.2}Sn_{0.2}Ti_{0.2}Hf_{0.2}Y_{0.2})O_{3-x}$ | Major | Minor | Trace | 13.3% | 0.95 |
| #S4 | $Sr(Zr_{0.2}Sn_{0.2}Ti_{0.2}Hf_{0.2}Ge_{0.2})O_3$ | Trace | Trace | Major | 11.2% | 0.99 |
| #S5 | $Sr(Zr_{0.2}Sn_{0.2}Ti_{0.2}Hf_{0.2}Nb_{0.2})O_3$ | Minor | Trace | No | 6.0% | 0.97 |
| #B0 | $Ba(Zr_{0.25}Sn_{0.25}Ti_{0.25}Hf_{0.25})O_3$ | Minor | Minor | Major | 6.7% | 1.03 |
| #B1 | $Ba(Zr_{0.2}Sn_{0.2}Ti_{0.2}Hf_{0.2}Mn_{0.2})O_3$ | Major | Major | Major | 11.2% | 1.05 |
| #B2 | $Ba(Zr_{0.2}Sn_{0.2}Ti_{0.2}Hf_{0.2}Ce_{0.2})O_3$ | No | Minor | Major | 11.9% | 1.01 |
| #B3 | $Ba(Zr_{0.2}Sn_{0.2}Ti_{0.2}Hf_{0.2}Y_{0.2})O_{3-x}$ | No | Major | Major | 13.3% | 1.01 |
| #B4 | $Ba(Zr_{0.2}Sn_{0.2}Ti_{0.2}Hf_{0.2}Ge_{0.2})O_3$ | Minor | Minor | Major | 11.2% | 1.05 |
| #B5 | $Ba(Zr_{0.2}Sn_{0.2}Ti_{0.2}Hf_{0.2}Nb_{0.2})O_3$ | No | Minor | Major | 6.0% | 1.03 |
| #$S_{0.5}B_{0.5}$5 | $(Sr_{0.5}Ba_{0.5})(Zr_{0.2}Sn_{0.2}Ti_{0.2}Hf_{0.2}Nb_{0.2})O_3$ | Minor | No | No | 6.0% | 1.00 |

We note that there are several definitions of high-entropy alloys [2], which may or may not be entropy-stabilized phases; here, we use the term "high-entropy" to refer to solid solutions that have high configuration entropies (specifically, ≥1.5$R$ per mole, where $R$ is the gas constant, following a definition used by Miracle et al. [28]).

Specifically, we partially substituted Ti of $SrTiO_3$, $BaTiO_3$ and $(Sr_{0.5}Ba_{0.5})TiO_3$ with several elements of equal molar fractions (1/4 or 1/5), selected from Zr, Sn, Hf, Mn, Nb, Ce, Ge and Y. Thirteen targeted compositions were selected and studied (Table 1). To synthesize specimens, appropriate amounts of purchased oxides were weighed to match the stoichiometry of the 13 targeted compositions (Supplementary Table S-I). The powders were blended and high energy ball milled (HEBM) in a $Si_3N_4$ vial in a SPEX 8000D mill for 6 h. To prevent overheating, the HEBM was stopped every 30 min to rest for 10 min. The milled powders were compacted into pellets in a 1/4 inch-diameter die at ~300 MPa (for ~120 s). The pellets were sintered in a tube furnace isothermally (5 °C/min ramp rate). Subsequently, most sintered specimens were cooled inside the furnace (power off), where the cooling rate was measured to be about 50 °C/min at 1500 °C and 10 °C/min at 1300 °C. Specimens were characterized by X-ray diffraction (XRD) utilizing a Rigaku diffractometer with Cu Kα radiation and scanning electron microscopy (SEM, FEI Phillips XL30) equipped with an energy dispersive X-ray spectroscopy (EDXS) detector. Selected specimens were characterized by aberration-corrected scanning transmission electron microscopy (AC STEM) using a 200 kV JEOL ARM-200F STEM with a CEOS Gmbh probe Cs corrector, for which TEM specimens were prepared by using a dual-beam FEI Scios focused ion beam (FIB).

We have investigated Composition #S1, $Sr(Zr_{0.2}Sn_{0.2}Ti_{0.2}Hf_{0.2}Mn_{0.2})O_3$, as our primary model system. XRD revealed the presence of a secondary phase in the specimen sintered at 1300 °C (Fig. 1(a)). With increasing sintering temperature, the amount of the secondary phase decreased. The $Sr(Zr_{0.2}Sn_{0.2}Ti_{0.2}Hf_{0.2}Mn_{0.2})O_3$ specimen sintered at 1500 °C exhibited a single cubic phase, with no trace of the secondary phase detectable by XRD (Fig. 1(a)) and EDXS elemental mapping (Fig. 1(b)). Fig. 1(b) shows that a Mn-enriched secondary phase was detected from the EDXS mapping in the specimen sintered at 1400 °C (for 10 h and furnace-cooled, as a standard sintering recipe adopted in this study), while this secondary phase was not detectable by XRD (Fig. 1(a)). To verify that this secondary phase formed at 1400 °C was not kinetically limited, we conducted two additional experiments (Fig. 1(c)). While a specimen sintered at 1500 °C for 2 h and air-quenched was homogeneous, this Mn-enriched phase precipitated out in the 1500 °C × 2 h + 1400 °C × 2 h specimen (Fig. 1(c)). The dissolution of the Mn-enriched secondary phase in the homogenous cubic perovskite solid solution at a higher temperature of 1500 °C may be explained as entropy driven; however, we also found that precipitation occurred at a higher temperature of 1500 °C in several Ba based multi-cation perovskites that were single phases at lower temperatures (Table 1). Thus, it is uncertain whether entropy is the main driving force for the precipitation/dissolution of secondary phases in these multi-cation perovskite solid solutions.

To further confirm the formation of the disordered solid solution perovskite phase, we also calculated the XRD pattern based on the standard kinematic diffraction theory and assuming equal and random

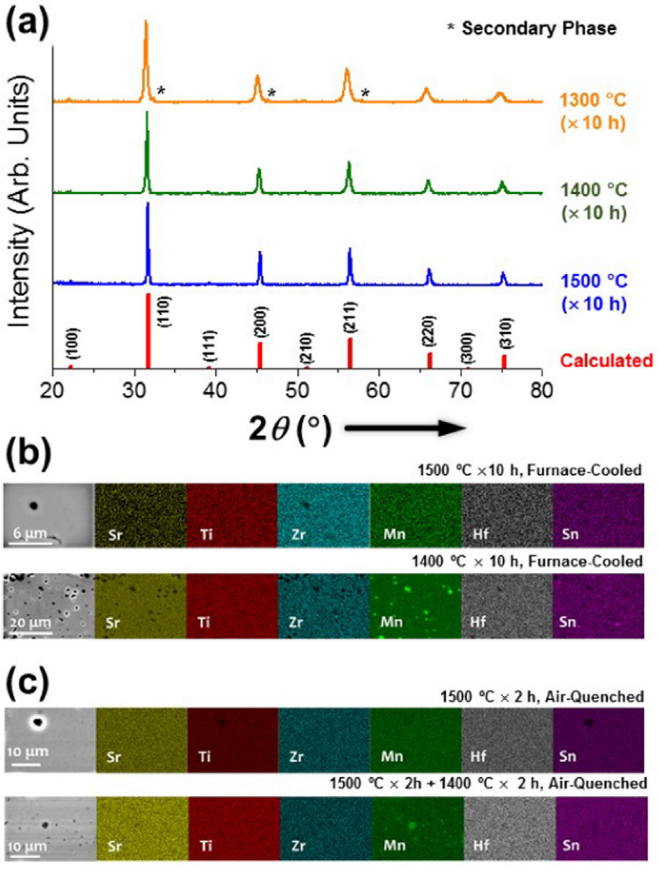


**Fig. 1.** (a) XRD patterns of $Sr(Zr_{0.2}Sn_{0.2}Ti_{0.2}Hf_{0.2}Mn_{0.2})O_3$ (Composition #S1) specimens sintered at different temperatures (isothermally for 10 h and furnace-cooled), along with a calculated XRD pattern assuming equal and random occupations of five cations on the B lattice site of a high-entropy perovskite crystal structure. Cross-sectional EDXS elemental maps of (b) selected standard sintered specimens (corresponding to those shown in (a)) and (c) air-quenched specimens to show that the Mn-enriched secondary phase formed at 1400 °C was not kinetically limited. (For interpretation of the references to color in this figure, the reader is referred to the web version of this article.)

occupations of five cations on the B lattice site of a cubic perovskite crystal structure, which agree well with experimental XRD pattern obtained from the specimen sintered at 1500 °C (shown by the blue *vs.* red patterns in Fig. 1(a)). The lattice constant (*a*) of the high-entropy perovskite phase formed at 1500 °C was measured to be 3.992 Å by XRD, which is close to calculated value of 4.032 Å (with ~1% in difference) from the rule of mixture (*i.e.*, the average lattice constant of five individual $ABO_3$ perovskites).

Fig. 2 shows STEM annular bright-field (ABF) and high-angle annular dark-field (HAADF) images of a single-phase $Sr(Zr_{0.2}Sn_{0.2}Ti_{0.2}Hf_{0.2}Mn_{0.2})O_3$ (Composition #S1) specimen sintered at 1500 °C, suggesting the compositional homogeneity at the nanoscale. The STEM images shown in Fig. 2 are consistent with the anticipated perovskite structure viewed along the $[00\bar{1}]$ zone axis; the lattice parameter *a* was measured to be 4.010 Å from STEM images, being close to the XRD value of 3.992 Å. The insets in Fig. 2(c) and 2(d) are the averaged images of STEM ABF and HAADF images (with an enlarged and colored image of averaged HAADF image being shown in Supplementary Fig. S14) [29–31], where the intensity reflects the Z (the atomic number of the atoms) difference of species and is roughly proportional to $Z^{1.7}$ [32,33]. The brightest spot in the HAADF image represents a column of "B ($Zr_{0.2}Sn_{0.2}Ti_{0.2}Hf_{0.2}Mn_{0.2}$) + O" atoms, while the adjacent, less bright, spots represent a column of A (Sr) atoms. The ratio of the maximum intensities of these two spots was measured to be 1.32 from the averaged HAADF image (Supplementary Fig. S14), which is close to the estimated ratio of (634 + 34)/485 ≈ 1.38 (Supplementary Table S-II) with <5% difference in the experimental and theoretical values. This again supports the formation of a homogenous $ABO_3$ solid solution without significant A-B anti-site defects.

All together, we have synthesized and characterized 13 compositions, including (i) two basic compositions #S0 and #B0, where we partially substituted Ti of $SrTiO_3$ and $BaTiO_3$ with Zr, Sn, and Hf; (ii) compositions #S1-#S5 and #B1-#B5, where we added a fifth component (Mn, Ce, Y, Ge or Nb) to the B site in #S0 and #B0, and (iii) Composition #$S_{0.5}$ $B_{0.5}$5 (discussed later). The specific compositions and key findings are summarized in Table 1; additional XRD and SEM-EDXS results are documented in Supplementary Figs. S1–S13. Interestingly, while both #S0 and #B0 (with four elements, Zr, Sn, Ti and Hf, of an equal molar fraction of ¼ on the B site) did not form single solid-solution phase at the temperature range of 1300–1500 °C (Table 1; Supplementary Figs. S1 and S7), adding a fifth element promoted the formation of single solid-solution phases in five compositions: #S1: $Sr(Zr_{0.2}Sn_{0.2}Ti_{0.2}Hf_{0.2}Mn_{0.2})O_3$ and #S5: $Sr(Zr_{0.2}Sn_{0.2}Ti_{0.2}Hf_{0.2}Nb_{0.2})O_3$ (*i.e.*, adding Mn/Nb to #S0) at 1500 °C, as well as #B2: $Ba(Zr_{0.2}Sn_{0.2}Ti_{0.2}Hf_{0.2}Ce_{0.2})O_3$, #B3: $Ba(Zr_{0.2}Sn_{0.2}Ti_{0.2}Hf_{0.2}Y_{0.2})O_{3-x}$ and #B5: $Ba(Zr_{0.2}Sn_{0.2}Ti_{0.2}Hf_{0.2}Nb_{0.2})O_3$ (*i.e.*, adding Ce/Y/Nb to #B0) at 1300 °C (Fig. 3 and Table 1). This suggests these solid-solution (high-entropy) perovskite phases (#S1, #S5, #B2, #B3 and #B5) to be entropy stabilized, at least to some extent.

The compositional uniformity of these (high-entropy) multi-cation perovskite solid solutions have been verified by EDXS compositional maps shown in Fig. 3(b). The lattice constants measured by XRD all agree well with those calculated from the rule of mixture (Supplementary Table-III). The experimental XRD patterns also agree well with

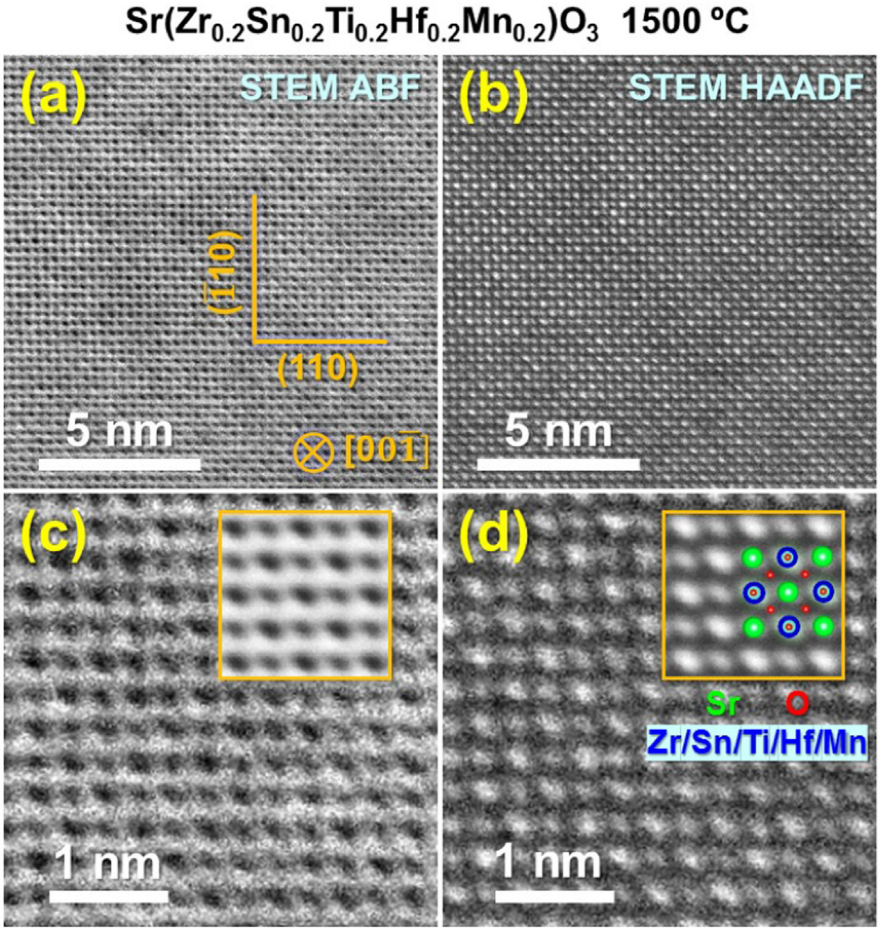


**Fig. 2.** Atomic-resolution STEM ABF and HAADF images of a representative high-entropy perovskite oxide, $Sr(Zr_{0.2}Sn_{0.2}Ti_{0.2}Hf_{0.2}Mn_{0.2})O_3$. (a, c) ABF and (b, d) HAADF images at (a, b) low and (c, d) high magnifications showing nanoscale compositional homogeneity and atomic structure. The $[00\bar{1}]$ zone axis and two perpendicular atomic planes (110) and $(\bar{1}10)$ are marked. Insets are averaged STEM images.

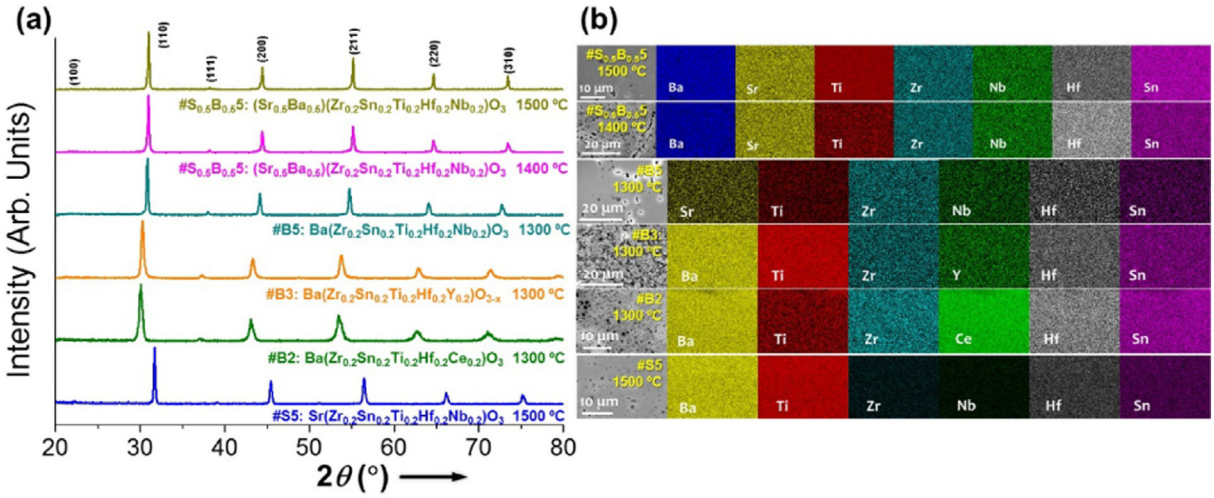


**Fig. 3.** (a) XRD patterns of five other compositions that form single-phase high-entropy perovskite oxides (at specific temperatures, labeled in the graph), where the peaks of the cubic perovskite phases are indexed. (b) The corresponding EDXS elemental maps, showing the compositional homogeneity.

calculated XRD patterns assuming equal and random occupations of five cations on the B lattice site. For the other compositions or sintering temperatures where secondary phases formed in the specimens, the primary phases are still cubic perovskite phases in most cases.

While A-B site mixing (anti-site defects) in any $ABO_3$ perovskite should inevitably exist due to an entropic effect, such anti-site defects should be insignificant in the current case because the large differences in the radii of the A and B site cations make the anti-site defects energetically unfavorable (since the radius of the A-site $Ba^{2+}$ or $Sr^{2+}$ cations is more than double of the average cation radius at the B site). This suggestion was further supported by the agreements between the simulated and experimental XRD patterns (as shown in Fig. 1(a) and Supplementary Figs. S1–S12) and an analysis of the intensity ratio of A and B sites in the HAADF image discussed above.

The atomic-size difference ($\delta$) is one factor that influences the formation of single high-entropy phases in metallic HEAs, where single solid solution phases appear to form in a region in the $\delta$-$\Omega$ plot ($\delta <$ ~6.5% and $\Omega >$ ~1, where $\Omega$ is a thermodynamic parameter that combines the effects of enthalpy of mixing, entropy of mixing and melting temperature; see a recent overview [2] and references therein). In the current case of perovskites, we (unfortunately) do not have the thermodynamic data to evaluate $\Omega$ that considers the entropy effects. Yet, we can define and evaluate a B-site cation-size difference as:

$$\delta(R_B) = \sqrt{\sum_{i=1}^{N} c_i \left(1 - R_{B_i} / \left(\sum_{i=1}^{N} c_i R_{B_i}\right)\right)^2} \quad (2)$$

where $R_{B_i}$ is the radius of the $i^{th}$ cation at the B site; $c_i$ is the mole fraction of the $i^{th}$ cation. Consequently, we have quantified $\delta(R_B)$ and list them in Table 1. We find that $\delta(R_B)$ are in the range of 6–12% for all cases studied here; furthermore, there is no obvious correlation between the calculated $\delta(R_B)$ and whether the compositions form single high-entropy perovskite phases. In fact, single high-entropy perovskite phases formed in several compositions with large cation-size differences, *e.g.*, $\delta(R_B) = 11.2\%$ for #S1, $\delta(R_B) = 11.9\%$ for #B2, and $\delta(R_B) = 13.3\%$ for #B3. Thus, the cation-size difference does not appear to be an important factor that determines the formation of single high-entropy perovskite phases in this case.

Interestingly, our experimental data suggest that the Goldschmidt tolerance factor ($t$), which has been calculated for all compositions using the average cationic radius on the B site ($\overline{R_B}$), listed in Table 1, appears to be a useful parameter. On one hand, the calculated tolerance factors for all six compositions that form single high-entropy perovskite phases are close to unity ($0.97 \le t \le 1.03$). On the other hand, six of the seven compositions that do not form single phases in the temperature range of 1300–1500 °C have $t \le 0.97$ or $t \ge 1.03$, with only one exception (Composition #S4, $t = 0.99$). This suggests that the Goldschmidt tolerance factor close to unity ($t \approx 1.00$) is perhaps a necessary, but not sufficient, criterion for forming a single high-entropy perovskite phase.

Yet another interesting observation is that the two Sr-based compositions (#S1, $t = 0.99$ and #S5, $t = 0.97$) that formed single perovskite solid-solution phases at a higher temperature of 1500 °C both have $t < 1$, whereas the three Ba-based compositions (#B2, $t = 1.01$; #B3, $t = 1.01$; and #B5, $t = 1.03$) that formed single perovskite solid-solution phases at a lower temperature of 1300 °C all have $t > 1$.

Finally, to further test the hypothesis that $t \approx 1$ should stabilize a single high-entropy perovskite phase, we examined Composition #$S_{0.5}B_{0.5}5$, $(Sr_{0.5}Ba_{0.5})(Zr_{0.2}Sn_{0.2}Ti_{0.2}Hf_{0.2}Nb_{0.2})O_3$, which is a 50%–50% solid solution of #S5 and #B5 that results in $t \approx 1.00$. Indeed, we found that single high-entropy perovskite phase formed in an extended temperature range, at both 1400 °C and 1500 °C, with only a minor amount of secondary phase at 1300 °C (Fig. 3; Table 1).

In summary, we have successfully synthesized six homogenous single-phase high-entropy $ABO_3$ perovskite oxides. The experiments suggested that the Goldschmidt tolerance factor close to unity ($t \approx 1.00$) is perhaps a necessary, but not sufficient, criterion to form a single high-entropy perovskite phase. Moreover, two Sr-based compositions that formed single solid-solution phases at the higher temperature of 1500 °C both have tolerance factors less than unity, whereas the three Ba-based compositions that formed single solid-solution phases at the lower temperature of 1300 °C all have tolerance factors greater than unity. A single solid-solution phase formed in $(Sr_{0.5}Ba_{0.5})(Zr_{0.2}Sn_{0.2}Ti_{0.2}Hf_{0.2}Nb_{0.2})O_3$ with $t \approx 1.00$ in an extended temperature range.

This study represents the first report of successful synthesis of high-entropy perovskite oxides (*i.e.* single solid-solution phases of multi-cation perovskite oxides with high configuration entropies of $\ge 1.5R$ per mole). Since $ABO_3$ perovskite oxides have many excellent physical properties with a broad range of applications, the discovery of this new class of multi-cation (high-entropy) perovskite solid solutions may allow simultaneous tailoring of multiple physical properties to meet challenging application requirements because of the vast compositional space that can be explored (including combinations of different cations, which can deviate from equal molar compositions to allow fine tunings). It is also possible that new functionality may be discovered in this new class of high-entropy solid solutions with drastically different chemistries, as compared with the conventional perovskite oxides.

## Acknowledgement

We acknowledge the partial supports from ONR-MURI (J.G., T.H., K.V. and J.L. *via* Grant No. N00014-15-1-2863 for the synthesis of high-entropy ceramics), NSF (J.N and J.L. *via* Grant No. CMMI-1436305 for investigating sintering and processing science of ceramics) and a Vannevar Bush Faculty Fellowship (T.H. and J.L. *via* ONR Grant No. N00014-16-1-2569 for the electron microscopy work).

## Appendix A. Supplementary data

Supplementary data to this article can be found online at http://dx.doi.org/10.1016/j.scriptamat.2017.08.040.

## References

[1] M.-H. Tsai, J.-W. Yeh, Mater. Res. Lett. 2 (2014) 107–123.
[2] D.B. Miracle, O.N. Senkov, Acta Mater. 122 (2017) 448–511.
[3] Y. Zhang, T. Zuo, Z. Tang, M.C. Gao, K.A. Dahmen, P.K. Liaw, Z. Lu, Prog. Mater. Sci. 61 (2014) 1–93.
[4] C.M. Rost, E. Sachet, T. Borman, A. Moballegh, E.C. Dickey, D. Hou, J.L. Jones, S. Curtarolo, J.-P. Maria, Nat. Commun. 6 (2015).
[5] D. Bérardan, S. Franger, A. Meena, N. Dragoe, J. Mater. Chem. A 4 (2016) 9536–9541.
[6] D. Bérardan, S. Franger, D. Dragoe, A.K. Meena, N. Dragoe, Phys. Status Solidi (RRL) 10 (2016) 328–333.
[7] J. Gild, Y. Zhang, T. Harrington, S. Jiang, T. Hu, M.C. Quinn, W.M. Mellor, N. Zhou, K. Vecchio, J. Luo, Sci Rep 6 (2016) 37946.
[8] V.M. Goldschmidt, Naturwissenschaften 14 (1926) 477–485.
[9] N. Ramadass, Mater. Sci. Eng. 36 (1978) 231–239.
[10] N.Q. Minh, J. Am. Ceram. Soc. 76 (1993) 563–588.
[11] K. Kreuer, Annu. Rev. Mater. Res. 33 (2003) 333–359.
[12] M.S. Wrighton, A.B. Ellis, P.T. Wolczanski, D.L. Morse, H.B. Abrahamson, D.S. Ginley, J. Am. Chem. Soc. 98 (1976) 2774–2779.
[13] N. Wang, M. Cao, Z. He, C. Diao, Q. Zhang, Y. Zhang, J. Dai, F. Zeng, H. Hao, Z. Yao, H. Liu, Ceram. Int. 42 (2016) 13593–13600.
[14] Z. Wang, M. Cao, Q. Zhang, H. Hao, Z. Yao, Z. Wang, Z. Song, Y. Zhang, W. Hu, H. Liu, J. Am. Ceram. Soc. 98 (2015) 476–482.
[15] J. Karczewski, B. Riegel, M. Gazda, P. Jasinski, B. Kusz, J. Electroceram. 24 (2010) 326–330.
[16] A.S. Bhalla, R.Y. Guo, R. Roy, Mater. Res. Innov. 4 (2000) 3–26.
[17] K.F. Wang, J.M. Liu, Z.F. Ren, Adv. Phys. 58 (2009) 321–448.
[18] W. Eerenstein, N.D. Mathur, J.F. Scott, Nature 442 (2006) 759–765.
[19] A.A. Bokov, Z.G. Ye, J. Mater. Sci. 41 (2006) 31–52.
[20] Y. Saito, H. Takao, T. Tani, T. Nonoyama, K. Takatori, T. Homma, T. Nagaya, M. Nakamura, Nature 432 (2004) 84–87.
[21] R.E. Cohen, Nature 358 (1992) 136–138.
[22] N. Reyren, S. Thiel, A.D. Caviglia, L.F. Kourkoutis, G. Hammerl, C. Richter, C.W. Schneider, T. Kopp, A.S. Ruetschi, D. Jaccard, M. Gabay, D.A. Muller, J.M. Triscone, J. Mannhart, Science 317 (2007) 1196–1199.
[23] A. Ohtomo, H.Y. Hwang, Nature 427 (2004) 423–426.
[24] Y. Maeno, H. Hashimoto, K. Yoshida, S. Nishizaki, T. Fujita, J.G. Bednorz, F. Lichtenberg, Nature 372 (1994) 532–534.
[25] C. Duan, J. Tong, M. Shang, S. Nikodemski, M. Sanders, S. Ricote, A. Almansoori, R. O'Hayre, Science 349 (2015) 1321–1326.
[26] R.J. Gorte, Science 349 (2015) 1290.
[27] L. Yang, S. Wang, K. Blinn, M. Liu, Z. Liu, Z. Cheng, M. Liu, Science 326 (2009) 126–129.
[28] D. Miracle, J. Miller, O. Senkov, C. Woodward, M. Uchic, J. Tiley, Entropy 16 (2014) 494.
[29] G.B. Winkelman, C. Dwyer, T.S. Hudson, D. Nguyen-Manh, M. Döblinger, R.L. Satet, M.J. Hoffmann, D.J.H. Cockayne, Appl. Phys. Lett. 87 (2005) 61911.
[30] A.I. Kirkland, W.O. Saxton, J. Microsc. 206 (2002) 1–6.
[31] W.O. Saxton, T.J. Pitt, M. Horner, Ultramicroscopy 4 (1979) 343–353.
[32] S.J. Pennycook, D.E. Jesson, Ultramicroscopy 37 (1991) 14–38.
[33] K. Ishizuka, Ultramicroscopy 90 (2002) 71–83.

**Supplementary Material**

# A New Class of High-Entropy Perovskite Oxides

*Sicong Jiang, Tao Hu, Joshua Gild, Naixie Zhou, Jiuyuan Nie, Mingde Qin, Tyler Harrington, Kenneth Vecchio, Jian Luo**

*E-mail address: jluo@alum.mit.edu (J. Luo).

**Supplementary Table S-I** Summary of chemicals used for the synthesis of various high-entropy oxides. $SrTiO_3$, $SrSnO_3$, $BaZrO_3$, $SrZrO_3$, $HfO_2$, $MnO_2$, $CeO_2$, BaO, and SrO (>99% purity) were purchased from Alfa Aesar; $BaTiO_3$, $GeO_2$, $Y_2O_3$, $NbO_2$, and $SnO_2$ (>99.5% purity) were purchased from Sigma-Aldrich.

| | Composition | Chemicals used (appropriate molar fractions to match stoichiometric compositions) | | | | | |
|---|---|---|---|---|---|---|---|
| #S0 | $Sr(Zr_{0.25}Sn_{0.25}Ti_{0.25}Hf_{0.25})O_3$ | | $SrSnO_3$ | $SrTiO_3$ | $SrZrO_3$ | SrO | $HfO_2$ |
| #S1 | $Sr(Zr_{0.2}Sn_{0.2}Ti_{0.2}Hf_{0.2}Mn_{0.2})O_3$ | $MnO_2$ | | | | | |
| #S2 | $Sr(Zr_{0.2}Sn_{0.2}Ti_{0.2}Hf_{0.2}Ce_{0.2})O_3$ | $CeO_2$ | | | | | |
| #S3 | $Sr(Zr_{0.2}Sn_{0.2}Ti_{0.2}Hf_{0.2}Y_{0.2})O_{3-x}$ | $Y_2O_3$ | | | | | |
| #S4 | $Sr(Zr_{0.2}Sn_{0.2}Ti_{0.2}Hf_{0.2}Ge_{0.2})O_3$ | $GeO_2$ | | | | | |
| #S5 | $Sr(Zr_{0.2}Sn_{0.2}Ti_{0.2}Hf_{0.2}Nb_{0.2})O_3$ | $NbO_2$ | | | | | |
| #B0 | $Ba(Zr_{0.25}Sn_{0.25}Ti_{0.25}Hf_{0.25})O_3$ | | SnO2 | $BaTiO_3$ | $BaZrO_3$ | BaO | |
| #B1 | $Ba(Zr_{0.2}Sn_{0.2}Ti_{0.2}Hf_{0.2}Mn_{0.2})O_3$ | $MnO_2$ | | | | | |
| #B2 | $Ba(Zr_{0.2}Sn_{0.2}Ti_{0.2}Hf_{0.2}Ce_{0.2})O_3$ | $CeO_2$ | | | | | |
| #B3 | $Ba(Zr_{0.2}Sn_{0.2}Ti_{0.2}Hf_{0.2}Y_{0.2})O_{3-x}$ | $Y_2O_3$ | | | | | |
| #B4 | $Ba(Zr_{0.2}Sn_{0.2}Ti_{0.2}Hf_{0.2}Ge_{0.2})O_3$ | $GeO_2$ | | | | | |
| #B5 | $Ba(Zr_{0.2}Sn_{0.2}Ti_{0.2}Hf_{0.2}Nb_{0.2})O_3$ | $NbO_2$ | | | | | |

**Supplementary Table S-II** Estimations of the relative contributions to the intensities of different sites in $ABO_3$ in STEM images for Composition #S1, where Z is the atomic number of the element.

| | A | B | | | | | O |
|---|---|---|---|---|---|---|---|
| | Sr | Ti | Zr | Sn | Hf | Mn | |
| Z | 38 | 22 | 40 | 50 | 72 | 25 | 8 |
| $Z^{1.7}$ | 485 | 191 | 529 | 773 | 1437 | 238 | 34 |
| Average $Z^{1.7}$ | 485 | 634 | | | | | 34 |

**Supplementary Table S-III** Summary of lattice constants of the six single-phase high-entropy perovskites. The rule of mixture values refer to the average lattice constants of five individual $ABO_3$ perovskites.

| | Compositions | Measured Lattice Constant (a/Å) | Rule of Mixture (a/Å) | Difference (Measured vs. Rule of Mixture) | Standard Deviation (of Five Cation Radii, Å) |
|---|---|---|---|---|---|
| #S1 | $Sr(Zr_{0.2}Sn_{0.2}Ti_{0.2}Hf_{0.2}Mn_{0.2})O_3$ | 3.992 | 4.032 | 1.0% | 0.07 |
| #S5 | $Sr(Zr_{0.2}Sn_{0.2}Ti_{0.2}Hf_{0.2}Nb_{0.2})O_3$ | 4.021 | 4.067 | 1.1% | 0.04 |
| #B2 | $Ba(Zr_{0.2}Sn_{0.2}Ti_{0.2}Hf_{0.2}Ce_{0.2})O_3$ | 4.192 | 4.198 | 0.2% | 0.09 |
| #B3 | $Ba(Zr_{0.2}Sn_{0.2}Ti_{0.2}Hf_{0.2}Y_{0.2})O_{3-x}$ | 4.179 | 4.205 | 0.6% | 0.10 |
| #B5 | $Ba(Zr_{0.2}Sn_{0.2}Ti_{0.2}Hf_{0.2}Nb_{0.2})O_3$ | 4.105 | 4.155 | 1.2% | 0.04 |
| #$S_{0.5}B_{0.5}5$ | $(Sr_{0.5}Ba_{0.5})(Zr_{0.2}Sn_{0.2}Ti_{0.2}Hf_{0.2}Nb_{0.2})O_3$ | 4.072 | 4.111 | 1.0% | 0.06 |

# #S0: $Sr(Zr_{0.25}Sn_{0.25}Ti_{0.25}Hf_{0.25})O_3$

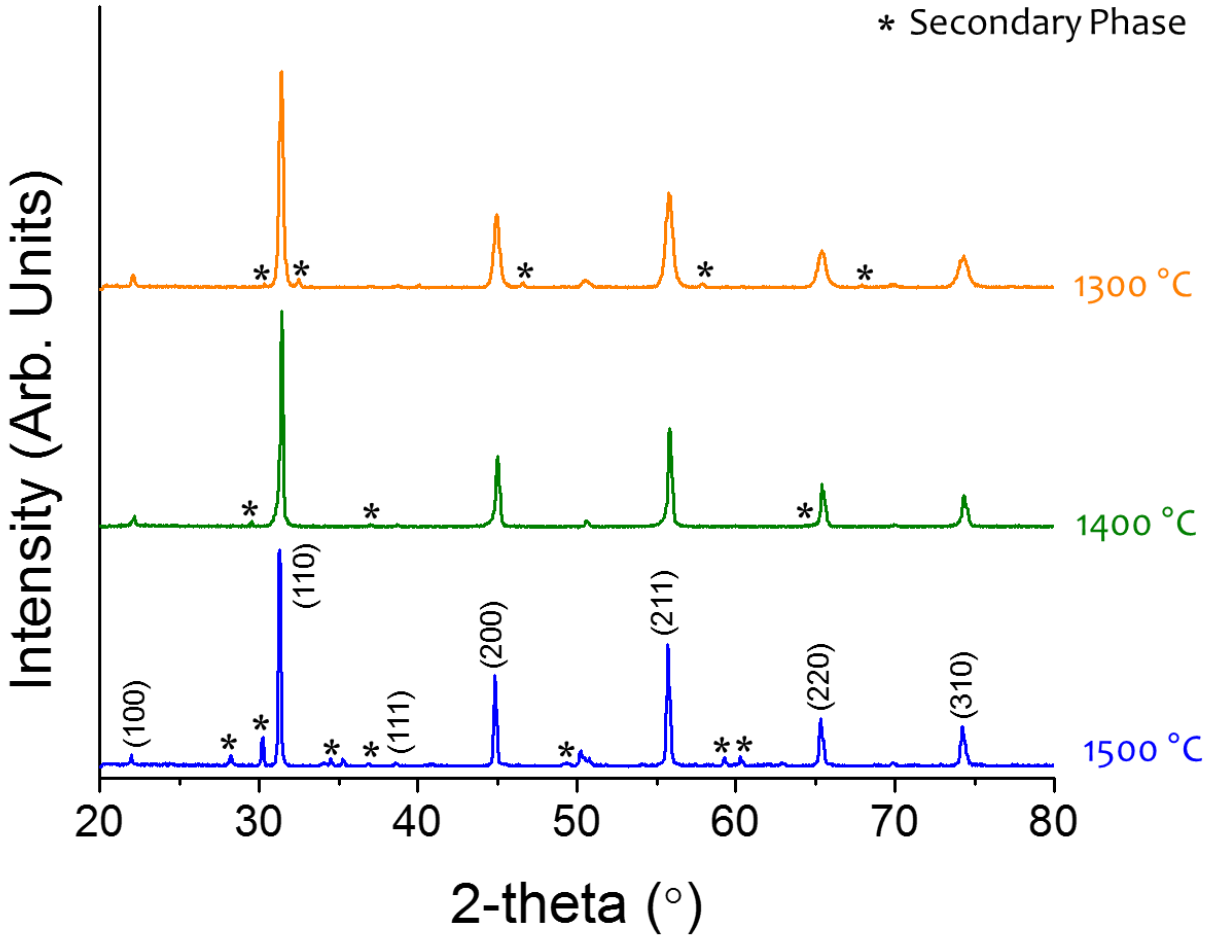


**Fig. S1.** XRD patterns of Composition #S0: $Sr(Zr_{0.25}Sn_{0.25}Ti_{0.25}Hf_{0.25})O_3$.

# #S1: $Sr(Zr_{0.2}Sn_{0.2}Ti_{0.2}Hf_{0.2}Mn_{0.2})O_3$

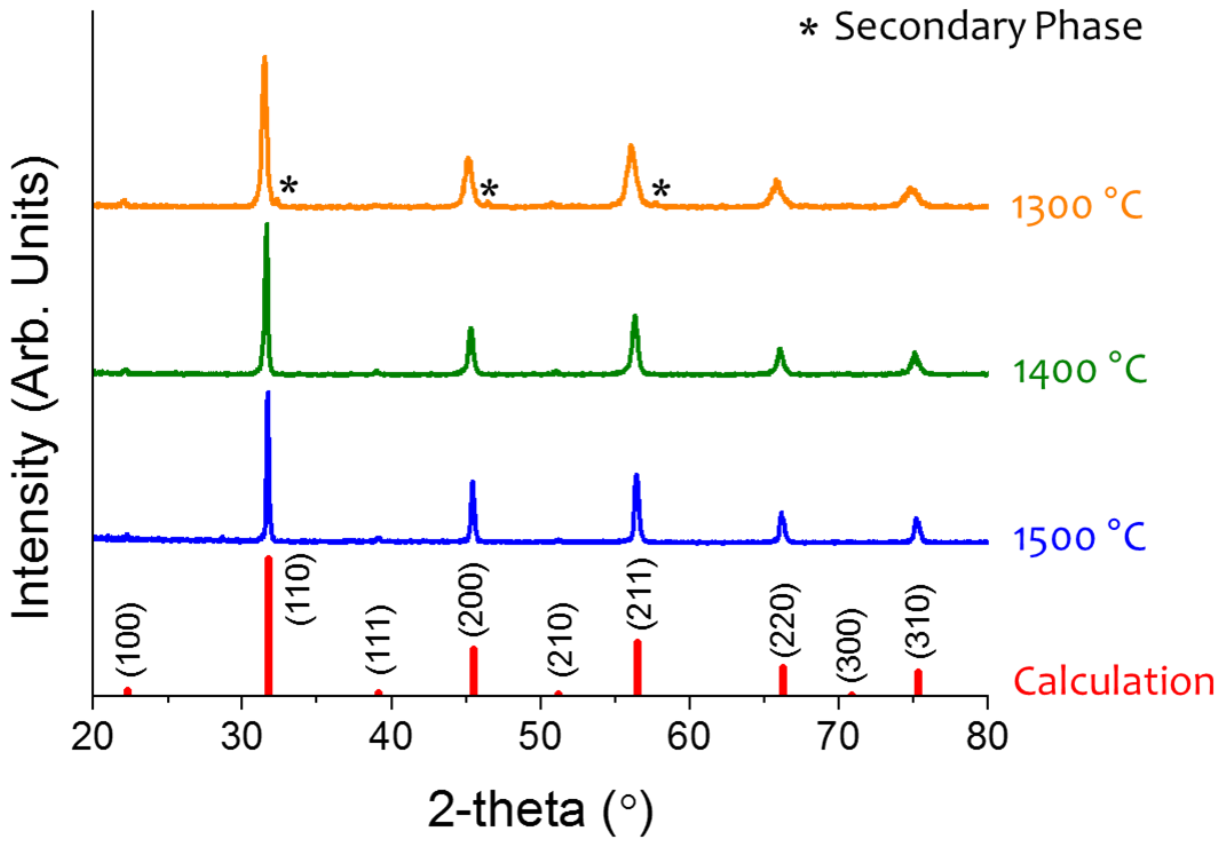


**Fig. S2.** XRD patterns of Composition #S2: $Sr(Zr_{0.2}Sn_{0.2}Ti_{0.2}Hf_{0.2}Mn_{0.2})O_3$.

# #S2: $Sr(Zr_{0.2}Sn_{0.2}Ti_{0.2}Hf_{0.2}Ce_{0.2})O_3$

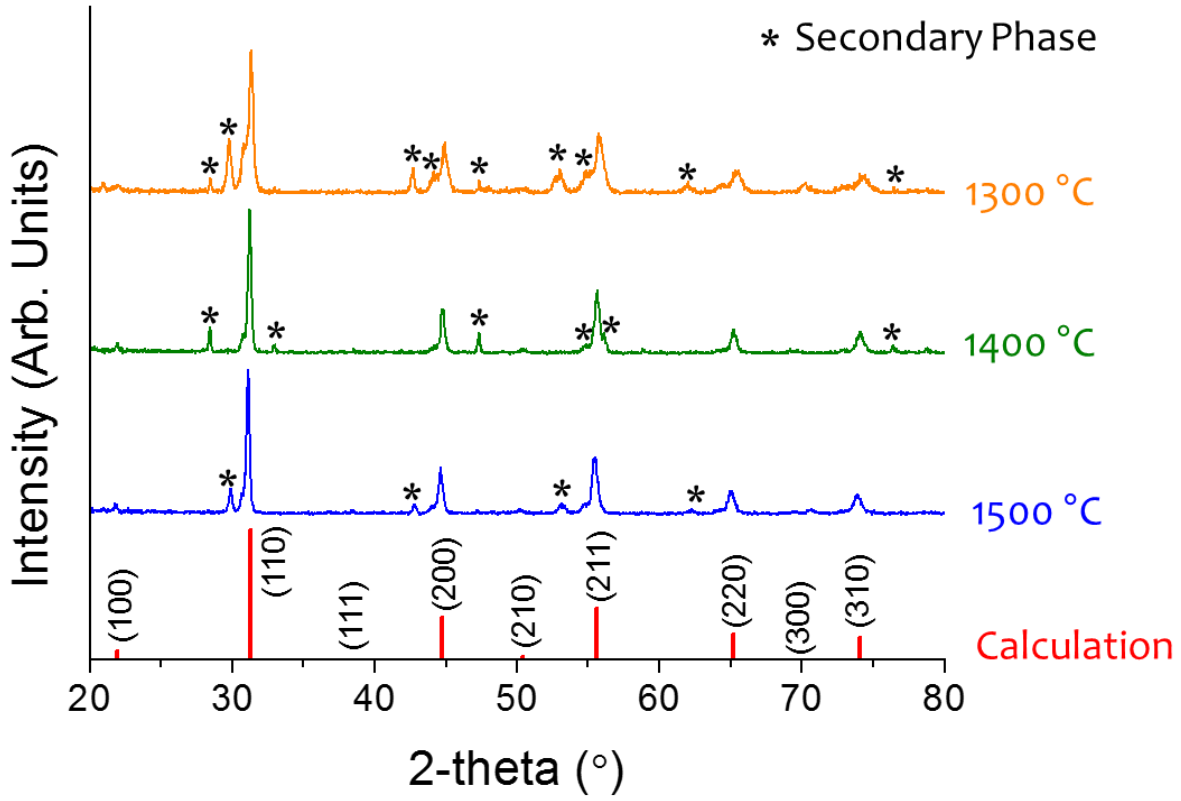


**Fig. S3.** XRD patterns of Composition #S2: $Sr(Zr_{0.2}Sn_{0.2}Ti_{0.2}Hf_{0.2}Ce_{0.2})O_3$.

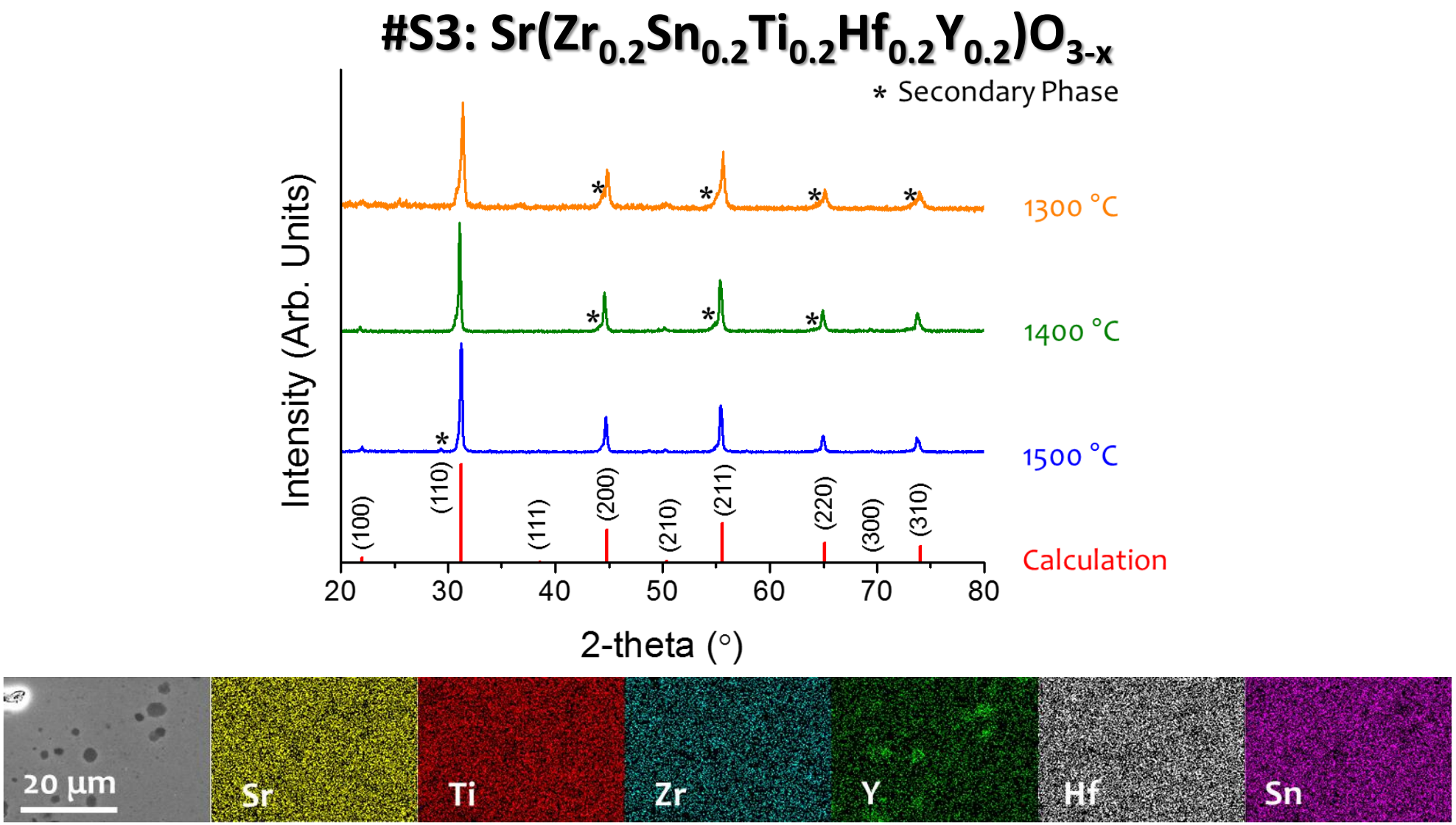


**Fig. S4.** XRD patterns of Composition #S3: $Sr(Zr_{0.2}Sn_{0.2}Ti_{0.2}Hf_{0.2}Y_{0.2})O_{3-x}$.
EDXS compositional maps of a #S3 specimen sintered at 1500 °C.

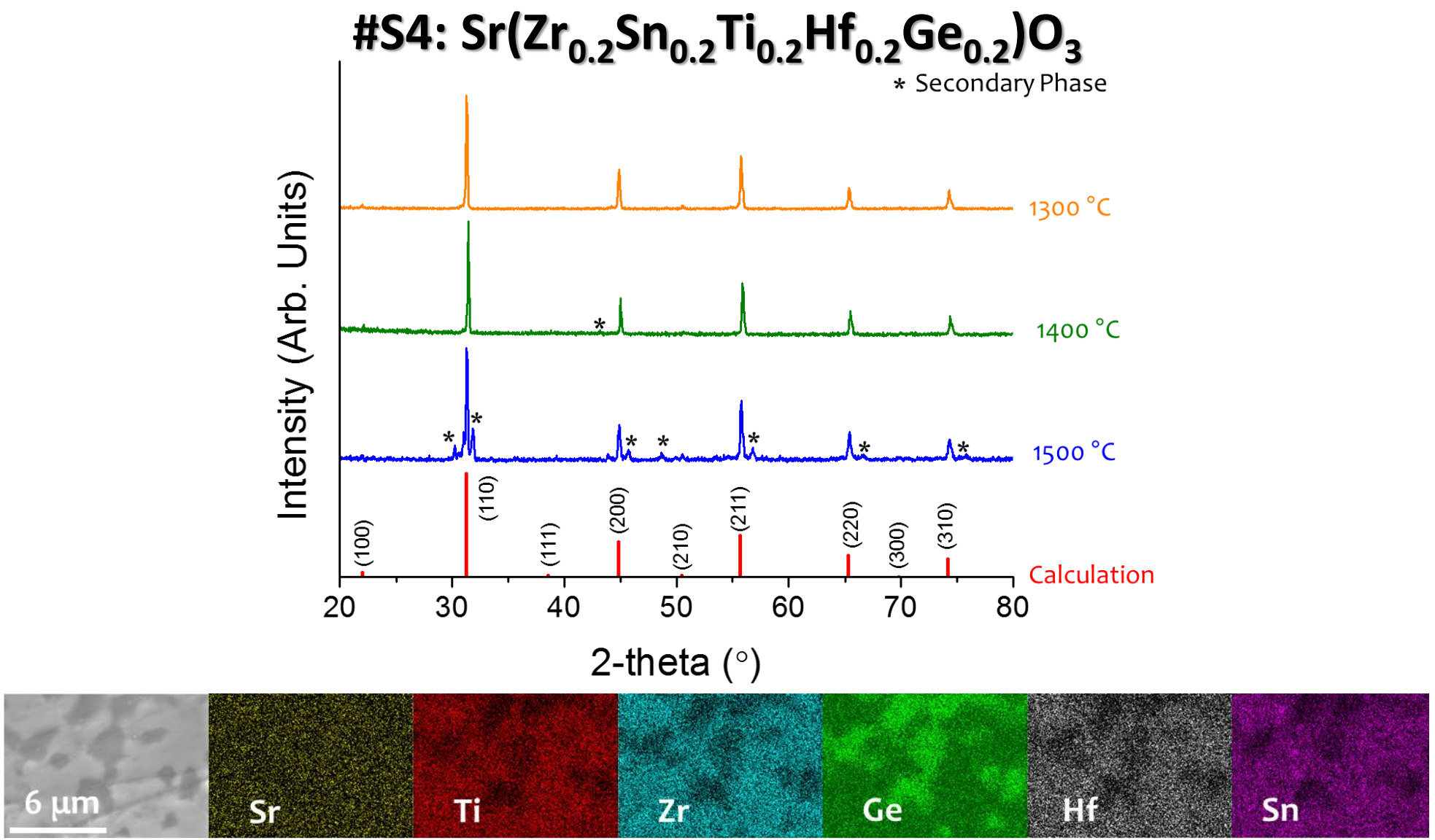


**Fig. S5.** XRD patterns of Composition #S4: $Sr(Zr_{0.2}Sn_{0.2}Ti_{0.2}Hf_{0.2}Ge_{0.2})O_3$. EDXS compositional maps of a #S4 specimen sintered at 1300 °C.

# #S5: $Sr(Zr_{0.2}Sn_{0.2}Ti_{0.2}Hf_{0.2}Nb_{0.2})O_3$

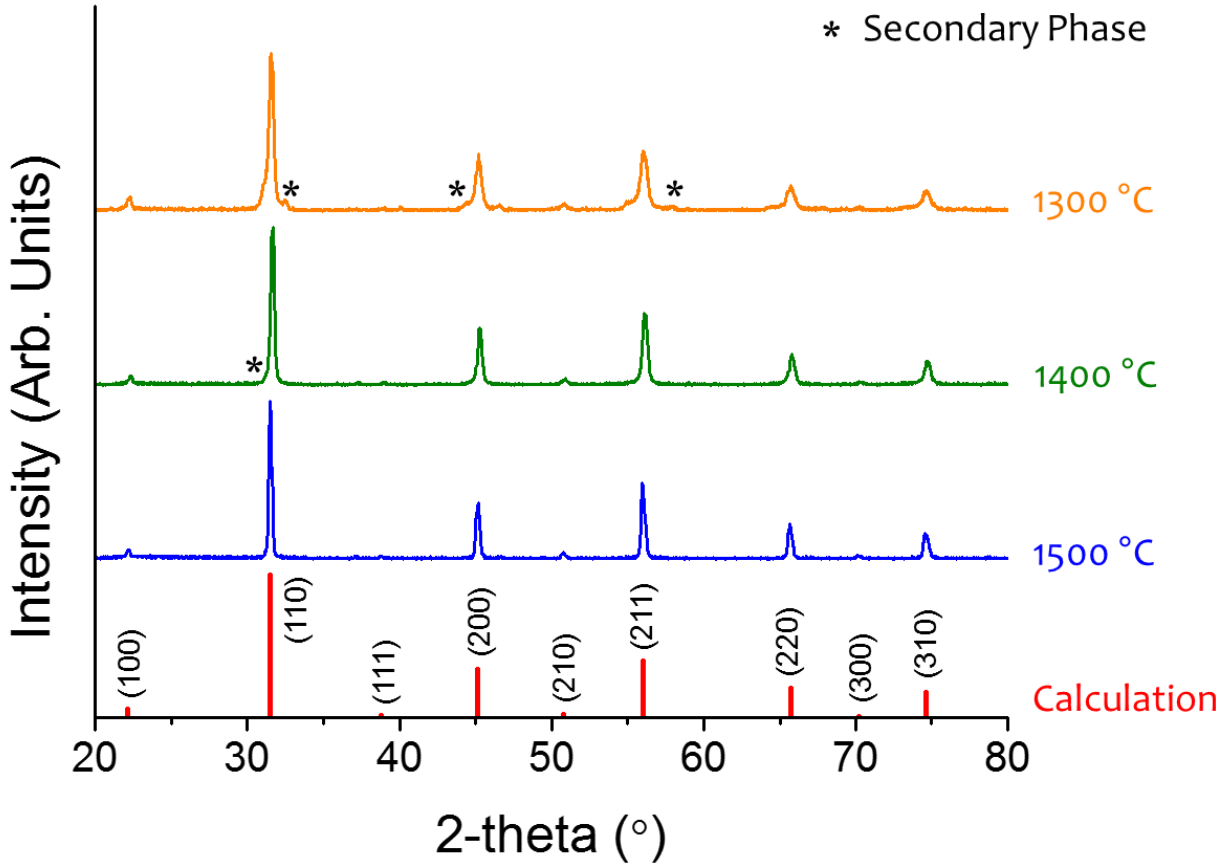


**Fig. S6.** XRD patterns of Composition #S5: $Sr(Zr_{0.2}Sn_{0.2}Ti_{0.2}Hf_{0.2}Nb_{0.2})O_3$.

# #B0: $Ba(Zr_{0.25}Sn_{0.25}Ti_{0.25}Hf_{0.25})O_3$

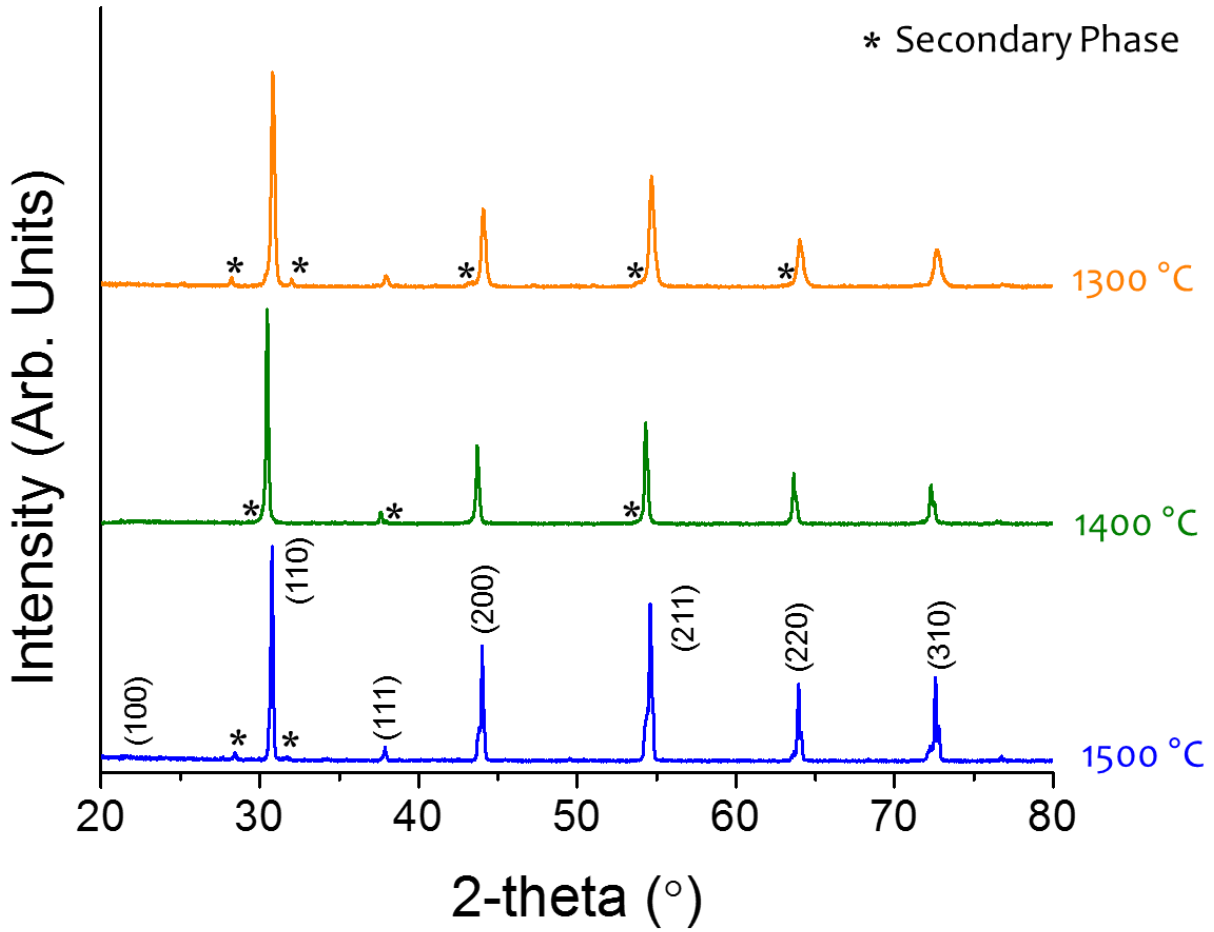


**Fig. S7.** XRD patterns of Composition #B0: $Ba(Zr_{0.25}Sn_{0.25}Ti_{0.25}Hf_{0.25})O_3$.

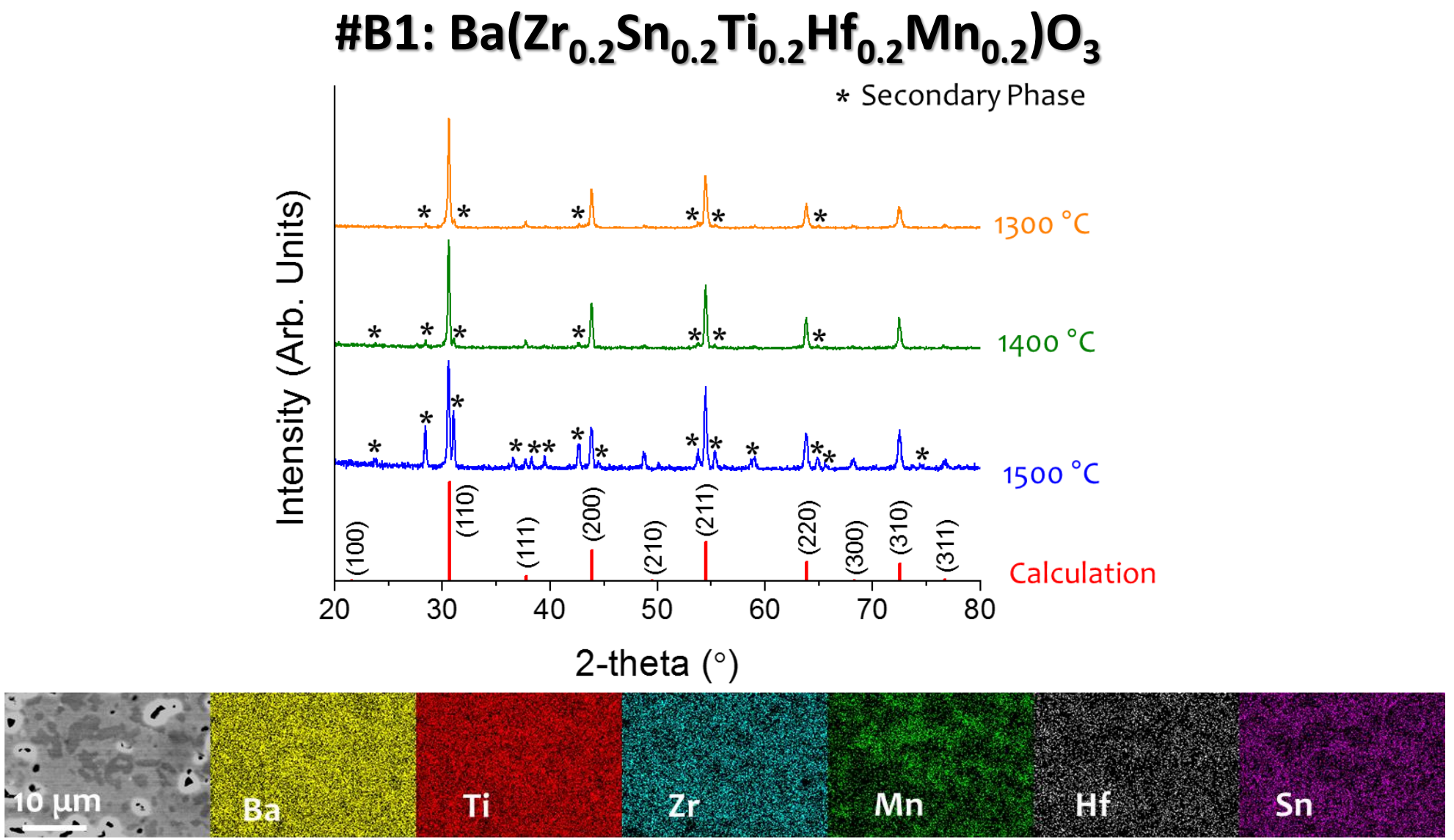


**Fig. S8.** XRD patterns of Composition #B1: $Ba(Zr_{0.2}Sn_{0.2}Ti_{0.2}Hf_{0.2}Mn_{0.2})O_3$. EDXS compositional maps of a #B1 specimen sintered at 1500 °C.

# #B2: $Ba(Zr_{0.2}Sn_{0.2}Ti_{0.2}Hf_{0.2}Ce_{0.2})O_3$

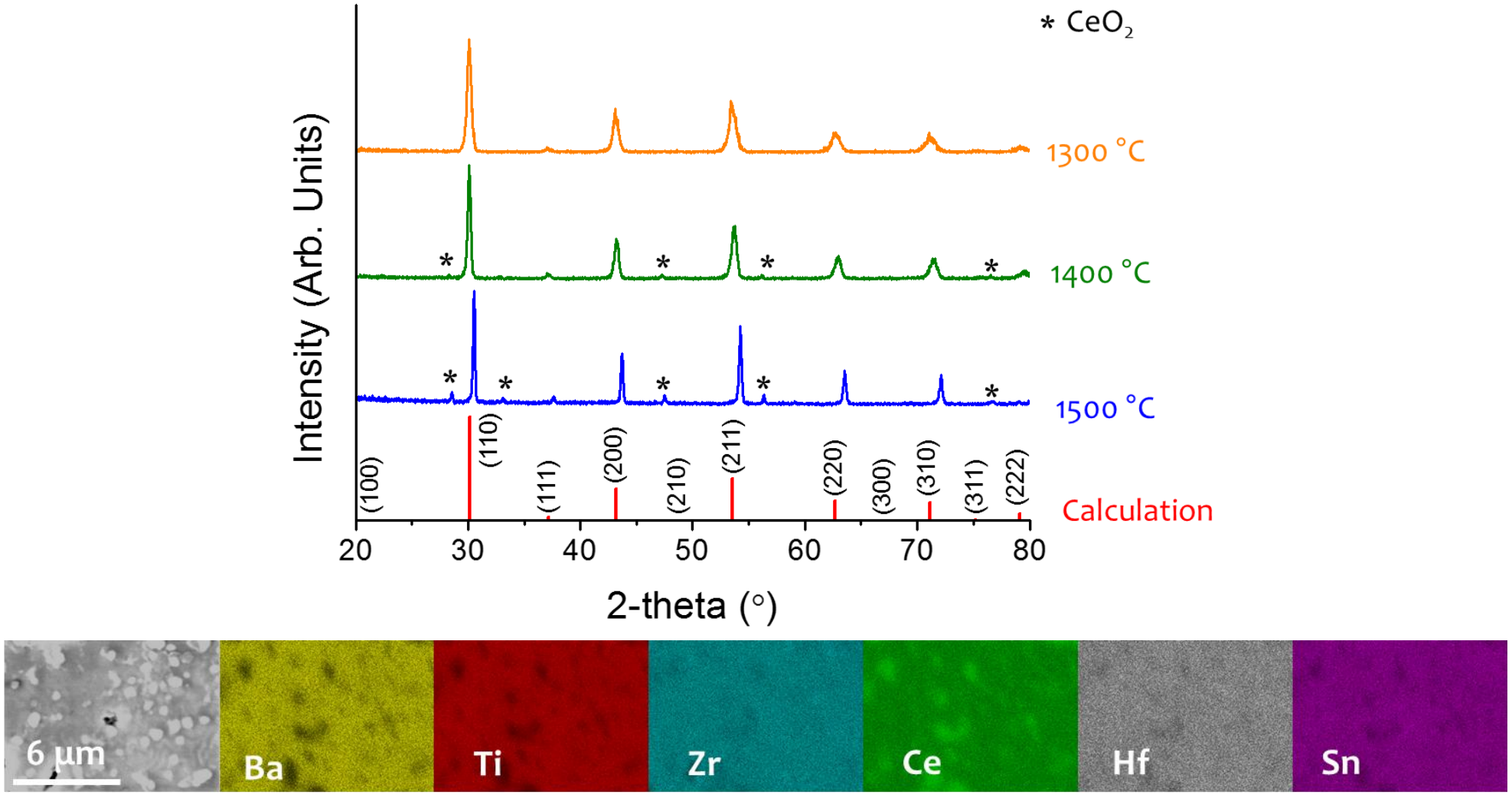


**Fig. S9.** XRD patterns of Composition #B2: $Ba(Zr_{0.2}Sn_{0.2}Ti_{0.2}Hf_{0.2}Ce_{0.2})O_3$. EDXS compositional maps of a #B2 specimen sintered at 1500 °C.

# #B3: $Ba(Zr_{0.2}Sn_{0.2}Ti_{0.2}Hf_{0.2}Y_{0.2})O_{3-x}$

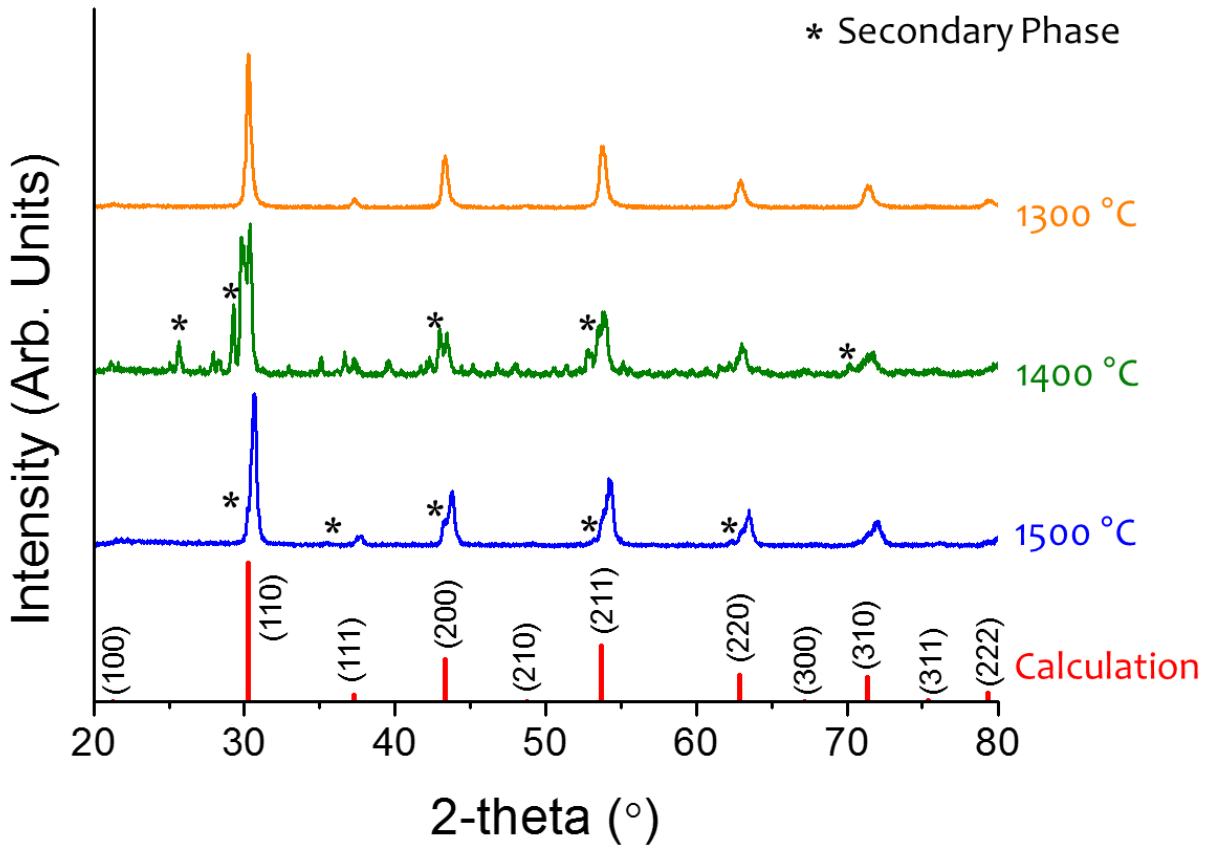


**Fig. S10.** XRD patterns of Composition #B3: $Ba(Zr_{0.2}Sn_{0.2}Ti_{0.2}Hf_{0.2}Y_{0.2})O_{3-x}$.

# #B4: $Ba(Zr_{0.2}Sn_{0.2}Ti_{0.2}Hf_{0.2}Ge_{0.2})O_3$

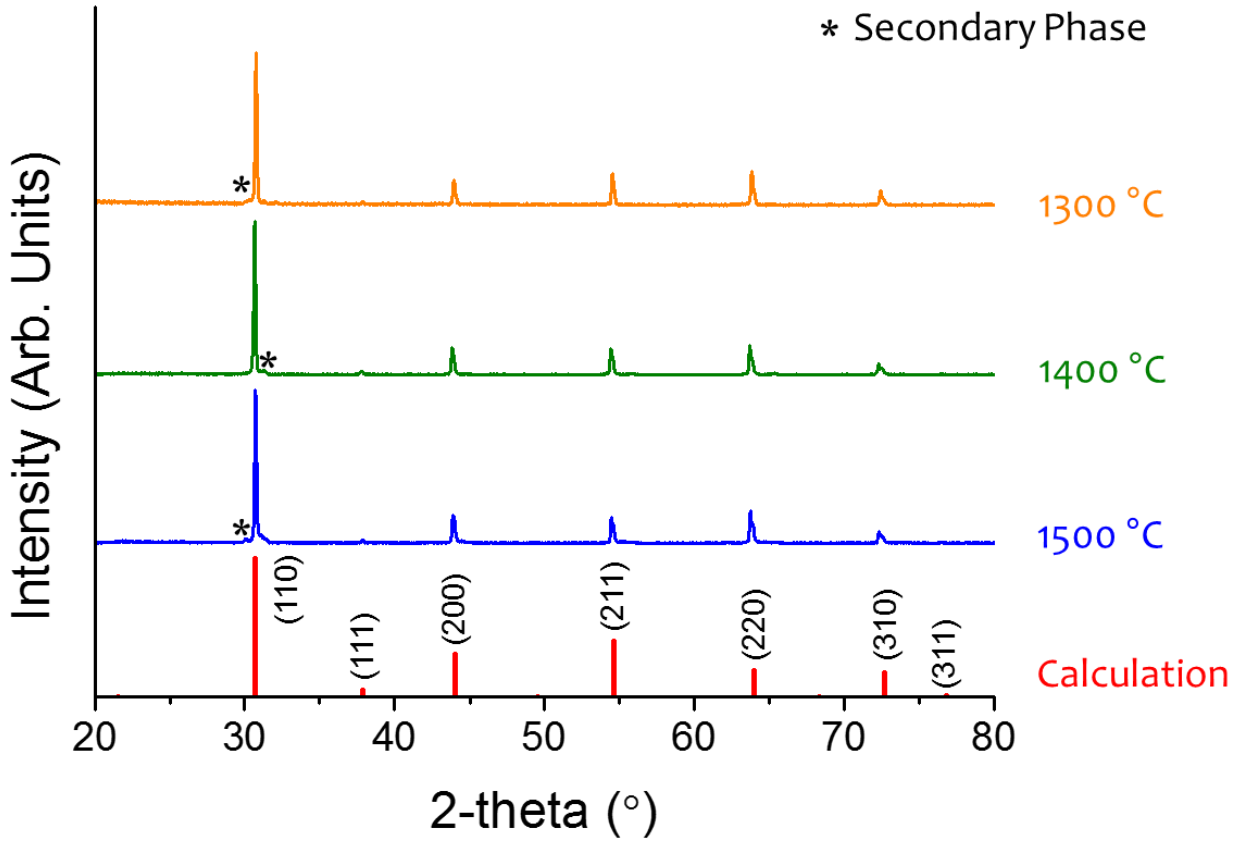


**Fig. S11.** XRD pattern of Composition #B4: $Ba(Zr_{0.2}Sn_{0.2}Ti_{0.2}Hf_{0.2}Ge_{0.2})O_3$.

# #B5: $Ba(Zr_{0.2}Sn_{0.2}Ti_{0.2}Hf_{0.2}Nb_{0.2})O_3$

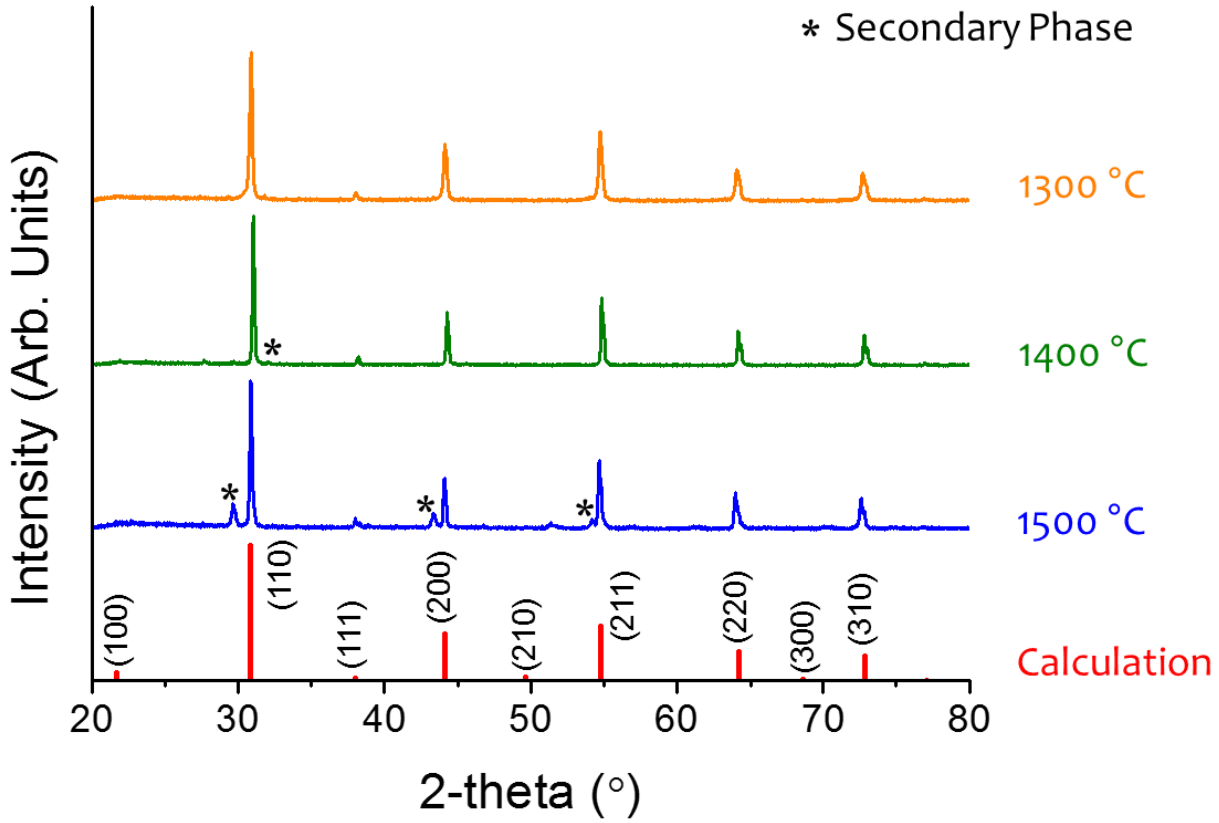


**Fig. S12.** XRD pattern of Composition #B5: $Ba(Zr_{0.2}Sn_{0.2}Ti_{0.2}Hf_{0.2}Nb_{0.2})O_3$.

# #$S_{0.5}B_{0.5}5$: $(Sr_{0.5}Ba_{0.5})(Zr_{0.2}Sn_{0.2}Ti_{0.2}Hf_{0.2}Nb_{0.2})O_3$

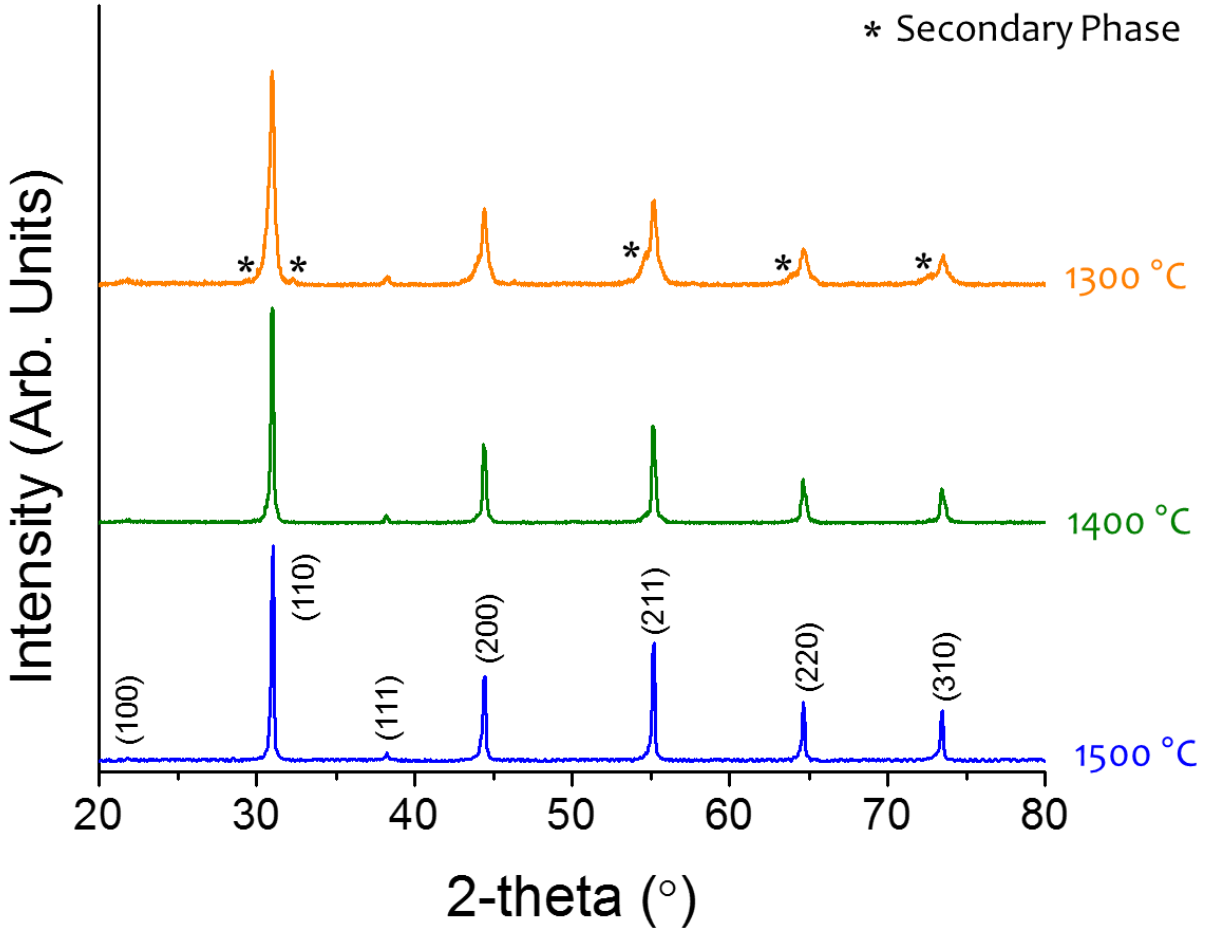


**Fig. S13.** XRD patterns of Composition #$S_{0.5}B_{0.5}5$: $(Sr_{0.5}Ba_{0.5})(Zr_{0.2}Sn_{0.2}Ti_{0.2}Hf_{0.2}Nb_{0.2})O_3$.

# Averaged HAADF Intensity

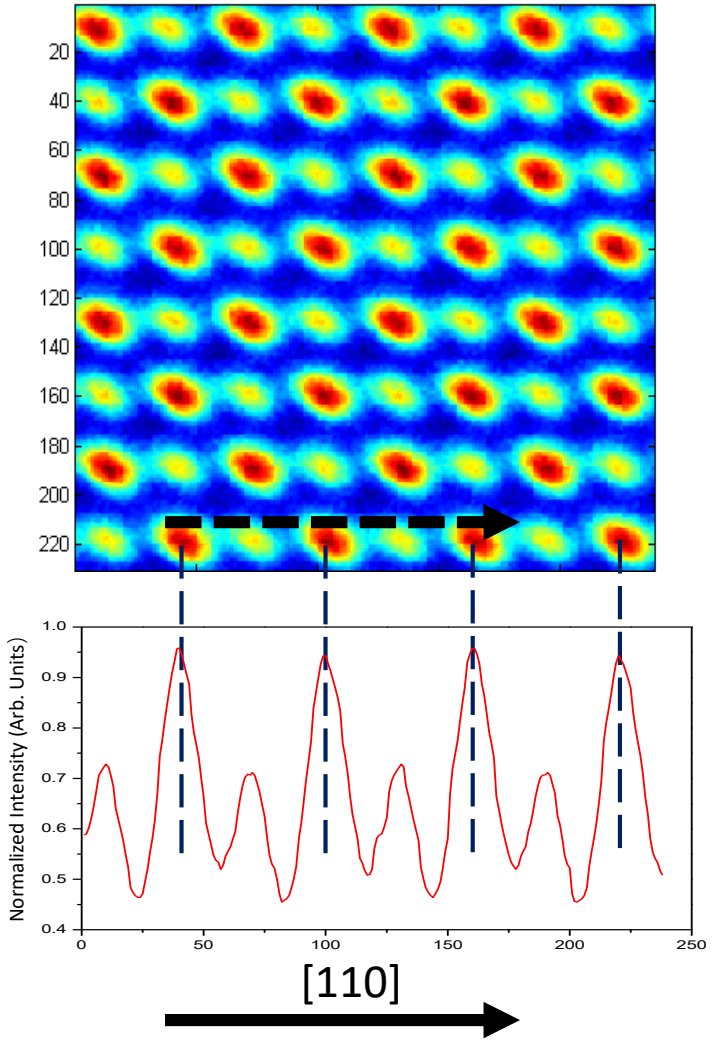


**Fig. S14.** Averaged HAADF intensity of Composition #S1: $Sr(Zr_{0.2}Sn_{0.2}Ti_{0.2}Hf_{0.2}Mn_{0.2})O_3$.